

FRICITION AND WEAR BEHAVIORS OF A HIGH NITROGEN AUSTENITIC STAINLESS STEEL Fe-19Cr-15Mn-0.66N

Y.-X. Qiao ^{a,*}, S.-L. Sheng ^a, L.-M. Zhang ^b, J. Chen ^{a,#}, L.-L. Yang ^a,
H.-L. Zhou ^a, Y.-X. Wang ^a, H.-B. Li ^c, Z.-B. Zheng ^{d,*#}

^a School of Materials Science and Engineering, Jiangsu University of Science and Technology, Zhenjiang, China

^b CAS Key Laboratory of Nuclear Materials and Safety Assessment, Institute of Metal Research, Chinese Academy of Sciences, Shenyang, China

^c School of Metallurgy, Northeastern University, Shenyang, China

^d Guangdong Key Laboratory of Metal Toughening Technology and Application, Guangdong Institute of Materials and Processing, Guangzhou, China

(Received 26 October 2020; Accepted 08 March 2021)

Abstract

The friction and wear behaviors of a Fe-19Cr-15Mn-0.66N high nitrogen austenitic stainless steel (HNSS) were investigated. Tribological investigations were carried out under different applied loads of 5 N, 10 N, 15 N, and 20 N. Scanning electron microscope (SEM) and laser scanning confocal microscope (LSCM) were used to understand the wear mechanisms under different loads and the reasons for the improved wear resistance. The lower friction coefficient and improved wear resistance were observed with the increase in applied loads. Under a higher load, the friction enhanced the work hardening ability of HNSS, which in turn improved its surface hardness and thus the increased wear resistance of HNSS.

Keywords: High nitrogen austenite stainless steel; Wear; Work hardening; Friction coefficient

1. Introduction

High nitrogen nickel-free stainless steels (HNSSs) have gained immense attention for various industrial applications owing to their high strength, good plasticity, excellent cavitation erosion resistance, and superior corrosion resistance [1-5]. For instance, HNSS can be used as bearing steel because it can overcome harsh service condition of high temperature, heavy load and high velocity due to improved wear resistance [6]. Better biocompatibility and wear resistance make the HNSS have the great potential as a biomedical material [7]. These desirable properties are mainly attributed to the addition of nitrogen (N) element. N has a strong ability to improve the strength of austenitic steels via solution strengthening, grain boundary hardening and strain hardening [8-11], and it can also enhance their pitting corrosion and wear resistance [12-15]. Some researchers have found that N, working with other alloying elements (i.e., Cr, Mo, V) together, can also improve the mechanical properties of steels [16, 17].

As a stabilizing element, N plays a vital role in stabilizing austenite phase. It has been reported that the ability of N element to stabilize austenite phase in the stainless steel is higher than that of Ni, and the stainless steels with solid solution N usually have high strength and good plasticity [18-21]. Therefore, all of these outstanding performances make the HNSS a promising engineering material.

Since friction is one of the main issues leading to material failure in service [22, 23], it is important to investigate the friction and wear behaviors of the HNSSs. Lin et al. researched the fretting wear performance of high-nitrogen stainless bearing steel (40Cr15Mo2VN) under lubrication conditions and found that the volume loss grew sharply because the wear mechanisms changed from abrasive wear to adhesion wear and finally to abrasive wear corresponding to the contact stress from 1.788 to 2.579 GPa [6]. Zhao et al. investigated the effect of cold deformation on friction property of nickel-free high nitrogen stainless steels in distilled water and Hank's solution, and results indicated that HNSS

Corresponding author: yxqiao@just.edu.cn ^{*}; jchen496@uwo.ca [#]; zbzhen712003@163.com ^{*#};



possessed excellent work-hardening capacity, and the dry wear rate decreased initially but subsequently increased due to increasing cold deformation [24, 25]. Vats et al. studied the tribo-corrosion behaviors of nickel-free high nitrogen austenitic stainless steel in simulated body fluids, and found that E_{corr} and i_{corr} values increased with the increase in load from 5 N to 10 N in Ringer's and artificial saliva solutions [26]. Mills et al. investigated the tribological behavior of a high-nitrogen Cr-Mn austenitic stainless steel and found that high nitrogen Cr-Mn steel performs better than AISI 304 in dry abrasion condition, high nitrogen Cr-Mn steel performed better than Hadfield manganese steel and AISI 304 stainless steel when tested in a corrosive environment [27]. In conclusion, the research on friction and wear behavior of HNSS is mainly focused on the deformation produced during production, lubrication and friction environment (e.g. human body, ocean). However, the effect of load on its tribological behavior at room temperature has hardly been investigated, while friction and wear will eventually occur in the practical use and will be significant [28-30].

In this work, the effect of applied load on the friction and wear properties of the HNSS was investigated and the wear mechanisms at different applied loads were revealed. The friction behaviors of a new-developed Fe-19Cr-15Mn-0.66N stainless steel were investigated using scanning electron microscopy, electron backscatter diffraction, and X-ray diffraction under different loads of 5 N, 10 N, 15 N and 20 N and the damage mechanisms were also discussed. This work provides a fundamental insight on the development of stainless steels with a higher wear resistance.

2. Experimental details

The HNSS used in present study is Fe-19Cr-15Mn-0.66N stainless steel which has been recently developed by Northeastern University, and its chemical composition (wt. %) is listed in Table 1. The raw materials were smelted in a JNL-172KL high vacuum furnace and casted into ingots, and then processed by forging, hot rolling, and cold rolling. After that, the processed material was cut into coupons with the dimension of 30 mm × 30 mm × 5 mm. Each sample was gradually ground using SiC paper up to 2000 grit, then polished using a diamond paste with diameter of 2.5 μm, cleaned in ethanol, and finally dried using cool air.

To characterize the elastic properties of the HNSS,

Table 1. Chemical composition of the HNSS used in present work (wt. %)

C	Si	Mn	P	S	Cr	N	Fe
0.044	0.24	15.80	0.017	0.005	18.40	0.66	Bal.

nanoindentation curves were acquired using a CSM NHT2 nanoindenter (Anton Paar) with a Berkovich tip at a maximum load of 20 mN and a loading/unloading rate of 40 mN·min⁻¹. The elastic behavior of material can be analyzed by its depth recovery ratio (η_h) obtained from the load-displacement curve [31], and the material with a better elastic property usually has a higher η_h value. The η_h value can be calculated as follows:

$$\eta_h = \frac{h_{\text{max}} - h_r}{h_{\text{max}}} \quad (1)$$

where h_{max} is the maximum penetration depth (nm), and h_r is the residual depth after unloading (nm) [32]. The nanoindentation experiments were repeated at least five times. The average value of five experiments was used as the test result, and the plus/minus ranges were calculated by calculating the standard deviation of five experimental data.

The friction test was conducted using an UMT-2 friction tester without lubrication, the schematic diagram of which is shown in Fig. 1. During the test, the pretreated samples were used as the working disk and the ceramic ball (Si_3N_4) as the friction couple. Under the action of the vertical load, the load was applied to the working disk, while the transverse load enabled the friction couple to reciprocate in a straight line through the motor. In the process of friction, the corresponding friction coefficient was calculated by transmitting data to the computer through the sensor on the loading rod. The tests were performed under dry conditions at the load of 5 N, 10 N, 15 N and 20 N and at a sliding speed of 0.025 m/s for 30 min corresponding to a sliding distance of 45 m.

The microstructure of the HNSS sample was characterized by scanning electron microscopy (SEM, JEOL, JSM-6480) and electron backscatter diffraction (EBSD, Oxford Instruments, NordlysNano Detector). The SEM was used the secondary electron (SE) imaging modes at an accelerating voltage of 20 kV and probe current of 50 pA. The step size of EBSD was 0.3 μm and the obtained EBSD data were processed and analyzed using the software HKL

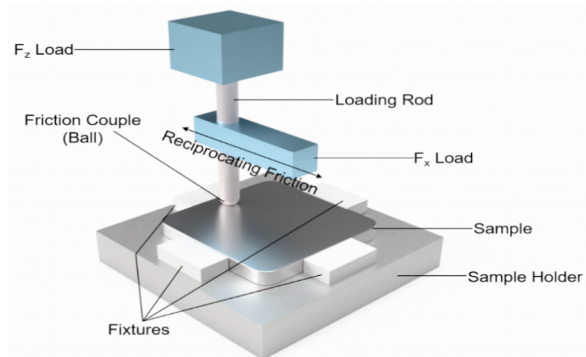


Figure 1. Schematic diagram of the friction tester used for friction test



Channel 5. X-ray diffraction (XRD, Rigaku Corporation, Tokyo, Japan) with Cu K α radiation was used at 10 kV and 35 mA to determine the phase present in the HNSS. The scan step size was 0.02 ° and the duration of each step was 2 s. After the friction test, the morphologies of wear scars and cross-section were observed using a laser scanning confocal microscope (LEXT, OLS400 LSCM) and SEM. Subsequently, the wear rates (W_s , mm³×N⁻¹×m⁻¹) can be calculated using Eq. 2:

$$W_s = \frac{CA}{FL} \quad (2)$$

where C is the length of the wear scar (mm), A is the average area of wear loss (mm²), F is the loading (N), and L is the distance of the wear (m) [33]. To investigate the effect of load on the hardness of the HNSS sample, the Vickers micro-hardness measurement was performed using an HXS-1000TAC tester with a load of 200 g and a load time of 20 s.

3. Results

3.1. Material characterization

Fig. 2 shows the EBSD images of the HNSS before friction test. It can be seen that the HNSS was mainly composed of austenite grain and some annealing twins were distributing inside of some austenite grains. The grain size ranged from 11 μ m to 55 μ m, making the average grain size to be 37 μ m. Generally, it is easy for austenitic stainless steel to form strain-induced martensite after cold deformation [34]. To determine the phase present in the HNSS, XRD was performed and the result is shown in Fig. 3, showing the presence of a single-phase austenite in the HNSS and the

absence of strain-induced martensite. The presence of the annealing twins observed in Fig. 2 is mainly attributed to the addition of high N content, since N can significantly reduce the stacking fault energy (SFE) of the HNSS [35] which made the annealing twins to form easily during the annealing process. Although some grains recrystallized after rolling, some of them were still present as subgrains with small sizes, which should be produced by grain refinement during the rolling process. The twins and the grain refinement can increase the hardness and strength of the HNSS based relevant investigation [36].

3.2. Nanoindentation test

The load–displacement curve of the HNSS acquired in the nanoindentation test is showed in Fig. 4. The maximum penetration depth (h_{max}) at a load of 20 mN and the residual depth after unloading (h_r) were 377.1 nm and 291.4 nm, respectively. According to Eq. 1, the

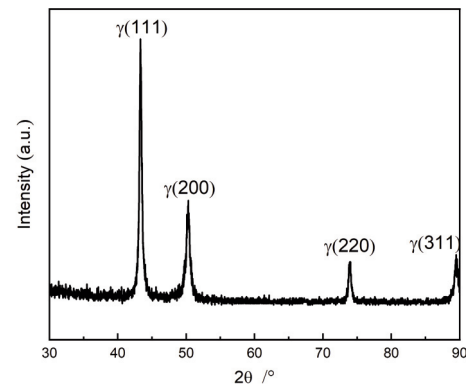


Figure 3. XRD pattern of the HNSS specimen

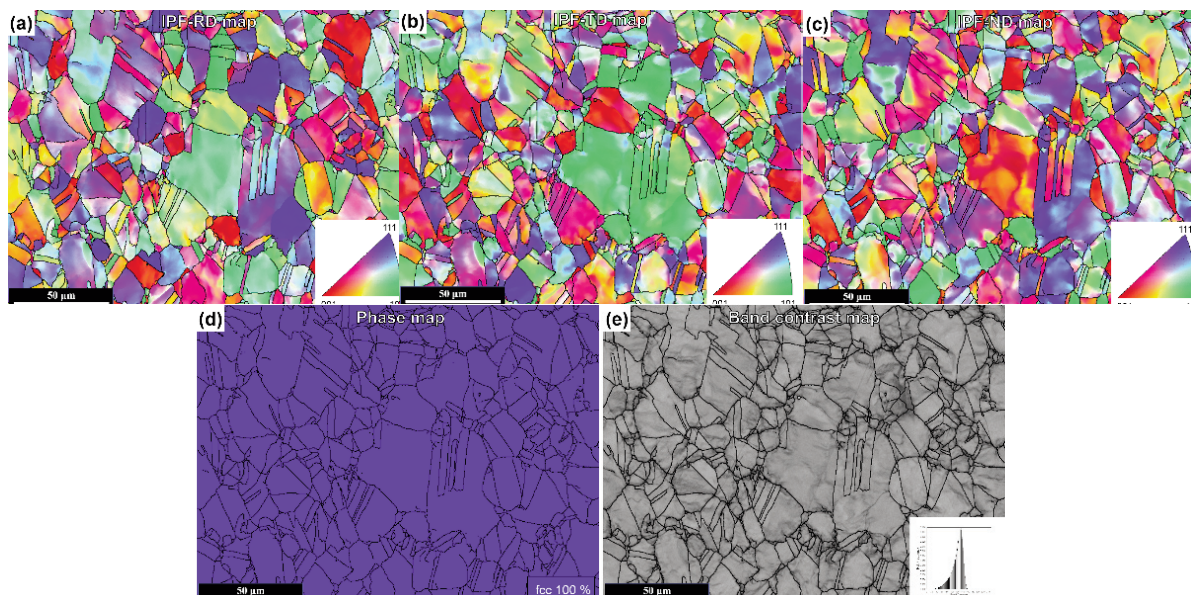


Figure 2. EBSD images of the HNSS matrix: **a** Inverse pole figure (IPF)-RD (rolling direction) map; **b** IPF-TD (transverse direction) map; **c** IPF-ND (normal direction) map; **d** phase map and **e** band contrast map

depth recovery ratio, η_h , of the HNSS is calculated to be 0.23. Besides this, the nanoindentation hardness can be determined according to the Oliver-Pharr method [37] and the calculated parameters are presented in Table 2.

3.3. Wear performance

Fig. 5 shows the plots of friction coefficient of the HNSS as a function of time under different loads. When the load was 5 N, the friction coefficient increased gradually upon the test periods of 600 s, and then fluctuated with the increasing time. The increase in the friction coefficient represented the transition from material intact to material fracture [38], whilst the variations of the friction coefficient were probably caused by the contact instability when the indenter plowed against the samples [39]. This phenomenon is in good agreement with the results of the published work [40, 41]. The maximum value of the friction coefficient could reach to 0.7. When the load increased to 10 N, the changes in the friction coefficient followed the same trend, but the variation amplitude became smaller compared with that under the load of 5 N. Under this circumstance, the maximum value of the friction coefficient was about 0.6. When the applied load was ≥ 15 N, the changes of the friction coefficients were similar. The friction coefficient increased rapidly at the initial stage (< 100 s), and then slightly fluctuated as the time increased, which yielded the maximum friction coefficient values of 0.56 and 0.54 under the load of 15 N and 20 N, respectively.

It is obvious that the friction coefficient decreased with the increase of applied load, suggesting that the variation of the friction coefficient may have been related to the wear mechanism caused by the change in the applied load [42]. Also, it can be noted that the

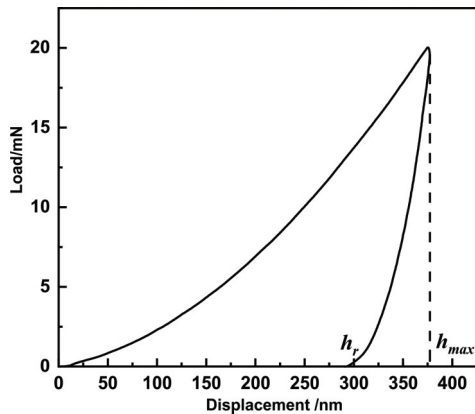


Figure 4. Load-displacement plot of the HNSS

Table 2. Indentation parameters derived from the load-displacement curve in Fig. 3

h_{max} (nm)	h_r (nm)	η_h	H_d (MPa)
369.61 ± 6.44	327.27 ± 7.79	0.12 ± 0.01	6504.32 ± 254.91

friction coefficient of the HNSS remained relatively stable under a higher load (i.e., 15 N and 20 N). The wear mechanisms of the HNSS would be interpreted based on the morphology observation in the wear scars, and would be explained in detail below.

The average friction coefficients of the tested samples under different applied loads are shown in Fig. 6. It is clear that the average friction coefficient steadily decreased with the increasing applied load, suggesting that the wear resistance of the HNSS sample increased as the applied load increased.

According to Eq. 2, the changes in the wear rate of the HNSS samples with the increase of applied load are shown in Fig. 7. It is clear that the wear rate decreased from $1.7 \times 10^7 \text{ mm}^3 \times \text{N}^{-1} \times \text{m}^{-1}$ to $3.4 \times 10^6 \text{ mm}^3 \times \text{N}^{-1} \times \text{m}^{-1}$ as the load increased from 5 N to 20 N.

3.4. Wear morphologies of HNSS

The results of friction coefficient and wear rate obtained are shown in Figs. 5-7, it showed that the wear resistance of the HNSS gradually enhanced with the increase of applied load. After the friction test, the wear surfaces and the cross-section of the HNSS samples under different loads were observed using

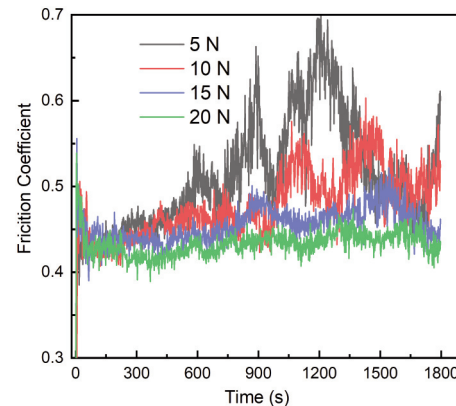


Figure 5. Plots of friction coefficient of HNSS against time under different applied loads

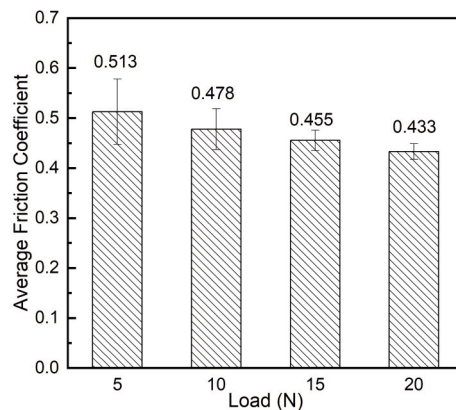


Figure 6. Average friction coefficient of the HNSS sample under different applied loads



LSCM. Fig. 8 clearly shows that the width of the wear scars increased progressively from 554 μm to 899 μm under a higher load, and the edges of the wear scars appear to be more uneven as the load increases. The friction between the friction couple and the HNSS caused the maximum radial stress on both sides of the wear track [43], leading to the initiation of cracks in the wear surface. Under higher loads (i.e., 15 N and 20 N), the higher frictional forces made these cracks grow at each side of the wear tracks in Fig. 8 c and d, leading to cohesive spallation [44]. Cross-sectional 2D topography of HNSS samples under different loads are shown in Fig. 9. As the load increases from 5 N to 20 N, the depth increases from 7 μm to 14 μm . It also shows obvious increase of the width of the wear scar, and the accumulation of the edge of the wear scar due to extrusion becomes more obvious as the load increases, which is consistent with the results of Fig. 8. When the applied loads are 15 N and 20 N,

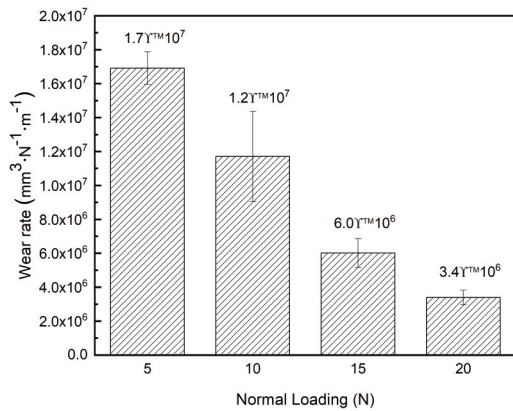


Figure 7. Wear rate of the HNSS sample under different applied loads

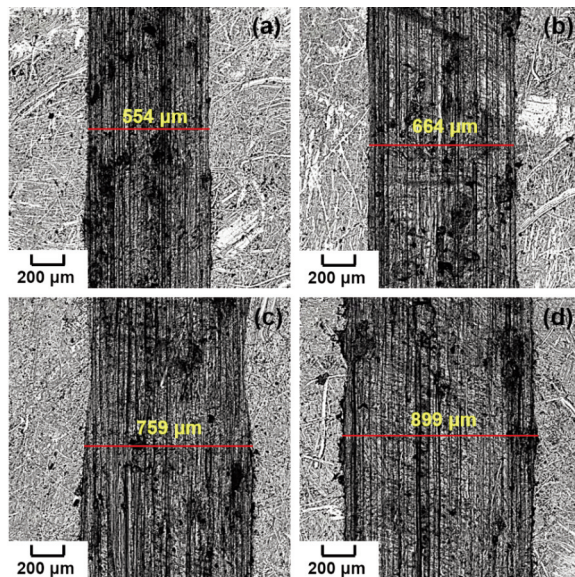


Figure 8. LSCM images of the wear scars under different applied loads: a 5 N, b 10 N, c 15 N, d 20 N

the widths and depths of the wear scars are similar and the profiles are only slightly different, and the sides of the profiles of 15 N and 20 N show much smoother compared with the profiles of wear scars of 5 N and 10 N, this exactly corresponds to the results of friction coefficient.

Fig. 10 presents the SEM morphologies of the HNSS under different applied loads. It can be seen that there were many defects observed such as grooves, wear debris, tearing, and delamination (as the arrows marked in Fig. 10). Based on the formation of these defects above, there were two wear mechanisms involved: abrasive wear and adhesive wear mechanism. When the loads were applied to the sample, the friction couple extruded the sample surface, leading to the plastic deformation of internal grains and eventually the nucleation and growth of cracks by cumulative plastic shear. Plentiful defects (i.e., grooves and wear debris) would form in the process of grain plastic deformation. The formation and propagation of the crack would lead to the detachment of materials. This micro-fracture process of materials is the typical process of abrasive wear [45]. During friction test, the local bonding between the HNSS sample and the friction couple occurred resulting in the formation of momentary micro-welding and tearing and eventually the material loss. This type of wear is known as adhesive wear. Thus, the wear resistance of a material is dependent on the resistance to deformation and fracture [24].

When the applied load was 5 N, there were many large scratches with grooves, tearing and delamination in the sliding direction, as shown in Fig. 10 a. The formation of the grooves in the sliding direction was due to the hard asperities of the counter-face [46], while tearing and delamination could be produced by the adhesion of the wear particles during their removal from the sample surface or/and their back transferring from the surface of friction couple [46]. A number of wear debris with various sizes were also observed, which were detached by plastic deformation [47]. As

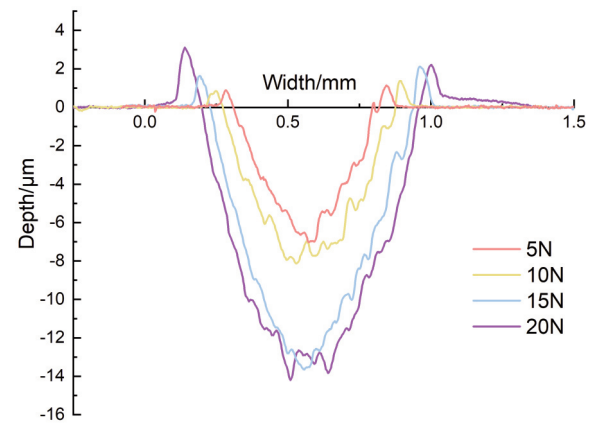


Figure 9. Two-dimensional (2D) profiles of cross section of the wear scars

the load increased to 10 N, the number of wear debris distributed in the grooves slightly decreased, as shown in Fig. 10 b. Under a higher applied load (i.e., 15 N or 20 N), this tendency of the decrease in wear debris number became more obvious, as shown in Figs. 10 c and d. The smooth appearance of the worn surface correlated well with the low friction coefficient, which was consistent with the previous work [42].

3.5. Micro-hardness measurements

Fig. 11 shows the cross-sectional micro-hardness profiles of the HNSS under different applied loads. It can be seen that the micro-hardness decreased from the sub-surface layer underneath the worn surface ($>450 \text{ HV}_{200}$) to the un-deformed base metal ($\sim 400 \text{ HV}_{200}$), suggesting that all samples experienced work hardening. According to the empirical electron theory of solids and molecules [48], the interstitial C, N and alloy element atoms can form many strong N(C)-Me covalent bond nets in the HNSS, which markedly hinder the dislocation movement and lattice reconfiguration process, thus improving the strength and work-hardening ability of the HNSS. High Mn and N content of the HNSS can reduce the SFE and facilitate the formation of the annealing twins. During the friction test, plastic deformation was accompanied by the increase of dislocation density, and the formation of twins during plastic deformation resulted in an increase in the resistance of dislocation slip, thus increasing the hardness [22, 49, 50]. The increase in the microhardness of the sub-surface layer underneath the worn surface indicates that the work-hardening rate increased with the increase of applied load. It is consistent with the previous work that the hardness of the HNSS increased after cold deformation as a consequence of the work-hardening effect [24, 32]. The work hardening behavior of the samples was more pronounced under a higher applied load, which could be

one of the reasons for higher wear resistance of HNSS as the load increased [51, 52].

4. Discussion

According to Hsu et al. [53], plastic deformation and its accumulation on the contacting asperities control the wear process when the temperature is ambient, and the tribological properties of the materials are closely related to their hardness.

At initial stages of the application of low load (i.e., 5 N and 10 N), the HNSS sample firstly had to experience elastic deformation (Fig. 4). The friction couple extruded the surface of HNSS, and the surface could be easily damaged, producing debris due to the low hardness [48], as demonstrated in Fig. 10 a and Fig. 12 a. Since it was difficult to embed these debris into the HNSS matrix in the process of reciprocating friction, these debris in turn would work together with the friction couple (Fig. 1) to wear the HNSS sample, leading to the formation of many grooves, as shown in Fig. 10 b. This is typical of

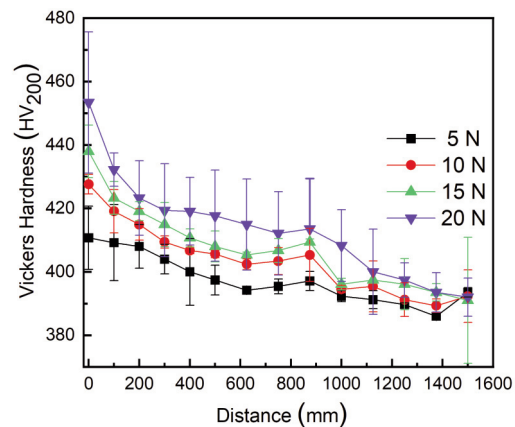


Figure 11. Cross-sectional hardness profiles of the HNSS under different applied loads

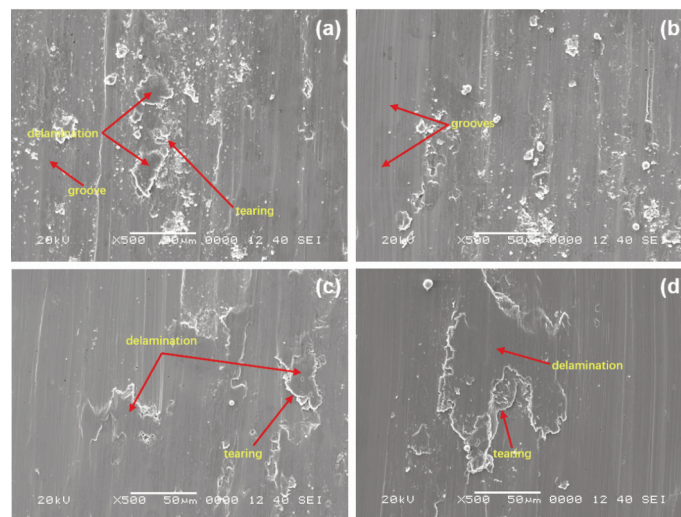


Figure 10. SEM of the worn surface under different applied loads: a 5 N, b 10 N, c 15 N, d 20 N

abrasive wear, Fig. 12 b. As the tribology process progressed, more and more debris/grooves were produced, making this ploughing process more severe but more unstable. Thus, the friction coefficient was high and fluctuated with the increasing time (Fig. 5). However, the further development of the ploughing process would lead to the increase of the friction strain of wear scars. As friction strain reached a critical value, the contacting asperities on worn surfaces started to yield to plastic deformation and finally fracture, leading to the formation of the stripping zone [54]. The stripping zones were transferred between the surface of wear scars and friction couples leading to adhesive wear. As a result, the wear mechanisms of the HNSS were abrasive wear and adhesive wear (Figs. 10 a and b) when the applied load is low (5 N or 10 N).

Under a higher applied load (i.e., 15 N and 20 N), it would be much easier for the HNSS sample to exceed the elastic deformation and experience plastic deformation. At initial stage of wear, the friction couple was pressed into the sample surface under the normal load, the contact area was abnormally small and the macroscopic contact stress was very large. When the friction couple moved relatively, it ploughed the wear surface with large friction resistance, resulting in high friction coefficient. With the progress of wear, the contact area between friction couple and the wear surface gradually increased, and the macroscopic contact stress decreased, thus the friction coefficient stabilized after the initial sharp increase [55] (Fig. 5). The changes in the friction coefficient (Figs. 5 and 6) indicate that the wear mechanism of the HNSS sample changed with the applied load. Under these circumstances, both the grooves and debris particles decreased (Figs. 10 c and d), but the area of plastic deformation increased due to higher hardness (Fig. 8). As the plastic deformation continued to develop, the micro-bulge on the surface of the HNSS sample was produced when the sample was in contact with the friction couple, and the friction force would push the shedding particles adhered to the surface of the sample, showing signs of delamination. Under

these circumstances, the wear mechanism of the HNSS sample was characteristic of adhesive wear mechanism [52].

During the friction and wear processes, work hardening can increase the hardness, strength, and deformation resistance of a material [56]. According to the changes in the friction behaviors of the HNSS samples and in the wear surface morphologies (Figs. 5-10), it is clearly stated that the hardness of the HNSS caused by work hardening during the friction test played a predominant role in the wear process [57]. After tribology test, both the micro-hardness of the HNSS sample underneath the wear scars and its work hardening rate increased with the increase in the applied load (Fig. 11), which was similar to the results obtained by Dib et al [58]. They found that the friction coefficient of AISI 304 stainless steel decreased with the load rise, which was attributed to the increased hardness, but the difference is that during the load increase, the hardness was increased mainly due to martensitic transformation, while the decrease of HNSS's friction coefficient was mainly due to the increase of hardness caused by work hardening. The increased micro-hardness raised the threshold for micro-cutting and decreased the fraction of material remove during the cutting regime [59]. Both the wear damage and the rate of the HNSS sample decreased with the increasing applied load, as displayed in Fig. 7 and Fig. 8. Fig. 7 shows a decreased wear rate of the HNSS as the load was increased from 5 N to 20 N, which could be attributed to the better work hardening performance of the HNSS during sliding under the higher normal loads enhancing the hardness and the strength of the substrate [54, 60]. The reason for the high work-hardening capacity of the HNSS was due to the effect of N and Mn (more than 15% in weight, Table 1) on the microstructures resulting in the reduction of the SFE [61, 62], which can not only promote the formation of twins [9, 63] (Fig. 2), but also make the dislocation configuration to change from wavy to planer dislocation. Also, the change of

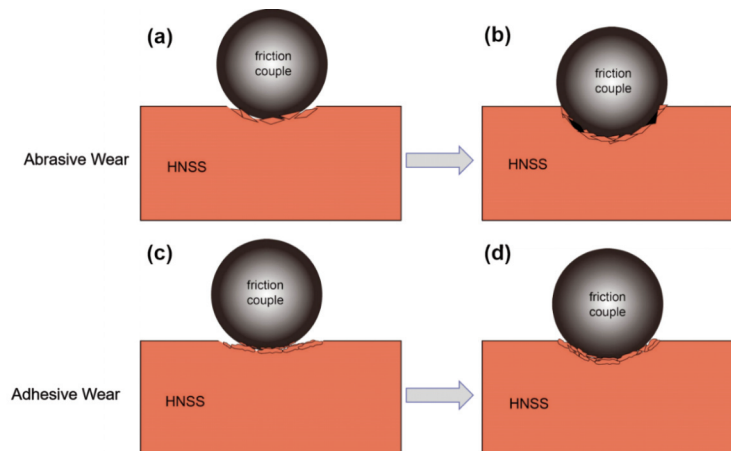


Figure 12. Schematic diagram of the wear mechanism a, b abrasive wear; and c, d adhesive wear

dislocation configuration reduced the chance of dislocations to cross-slip [64], thus improving the validity of planer dislocation. The fixed Lomer-Cottrell dislocations were formed at the intersection of planer dislocations, and further plastic flow was hindered as the higher loads were applied, which became the obstacle of subsequent dislocations, thus significantly increasing the work hardening tendency and wear resistance of the HNSS [10,48].

5. Conclusions

In this work, the friction and wear behaviors of Fe-19Cr-15Mn-0.66N high nitrogen austenitic stainless steel at different loads were investigated with Si₃N₄ ball as friction couple. The influences of load on wear morphologies were analyzed. The main conclusions of this work can be summarized as follows:

With the applied load increased from 5 N to 20 N, the friction coefficient of the Fe-19Cr-15Mn-0.66N austenitic stainless steel decreased from 0.51 to 0.43, indicating the increase in wear resistance.

The wear resistance of the HNSS was higher under a higher applied load due to the increased micro-hardness of the deformed HNSS caused by the formed work hardening layer and the increased work hardening rate.

When the applied load increased from 10 N to 15 N, the wear mechanism of the HNSS changed from mixed abrasive wear and adhesive wear to adhesive wear due to the increased hardness caused by work hardening, which was verified by the decrease of grooves and debris on the wear surfaces.

Acknowledgement

The authors acknowledge the financial support of the National Natural Science Foundation of China (Nos. 51905110 and 51401092), Science and Technology Planning Project of Guangzhou (No. 201906040007).

References

- [1] H.Y. Ha, T.H. Lee, C.S. Oh, S.J. Kim, Scripta Mater., 61 (2) (2009) 121-124.
- [2] G. Stein, I. Hucklenbroich, Mater. Manuf. Process., 19 (1) (2004) 7-17.
- [3] Y.X. Qiao, Z.H. Tian, X. Cai, J. Chen, Y.X. Wang, Q.N. Song, H.B. Li, Tribol. Lett. 67 (1) (2019) 1.
- [4] S.X. Jin, H.L. Ma, E.Y. Lu, L. Zhou, Q.L. Zhang, P. Fan, Q.Z. Yan, D.Q. Yuan, X.Z. Cao, B.Y. Wang, Mater. Energy Today, 20 (2021) 100687.
- [5] Y.X. Qiao, S. Wang, B. Liu, Y.G. Zheng, L.H. Bing, Z.H. Jiang, Acta Metall. Sin. 52 (2) (2016) 233-240.
- [6] H. Lin, M.S. Yang, B.P. Shu, J. Iron Steel Res. Int., 27 (7) (2020) 849-866.
- [7] M. Becerikli, H. Jaurich, C. Wallner, J. M. Wagner, M. Dadras, B. Jettkant, F. Pöhl, M. Seifert, O. Jung, B. Mitevski, A. Karkar, M. Lehnhardt, A. Fischer, M. D. Kauther, B. Behr, Plos One, 14 (3) (2019) e0214384.
- [8] H. HaEnninenena, J. Romu, R. Ilolaa, J. Tervoc, A. Laitinend, J. Mater. Process. Tech., 117 (3) (2001) 424-430.
- [9] P. Milliner, C. Solenthaler, P. Uggowitzer, M.O. Speidel, Mater. Sci. Eng. A, 164 (1-2) (1993) 164-169.
- [10] S. Kubota, Y. Xia, Y. Tomota, ISIJ Int., 38 (5) 474-481 (1998).
- [11] Y.M. Lin, Lu, J., L.P. Wang, T. Xu, Q.J. Xue, Acta Mater., 54 (20) (2006) 5599-5605.
- [12] R.F.A. Jargelius-Pettersson, Corros. Sci., 41 (8) (1999) 1639-1664.
- [13] H.J. Grabke, ISIJ Int., 36 (7) (1996) 777-786.
- [14] W.J. Simmons, Metall. Mater. Trans. A, 26 (10) (1995) 2579-2595.
- [15] Y.X. Qiao, Y.P. Chen, L.L. Li, W. Emori, J. Chen, X.J. Wang, L.L. Yang, H.L. Zhou, G. Song, N. Naik, Z.B. Wang, Z.H. Guo, JOM, 73 (2021). <https://doi.org/10.1007/s11837-021-04569-2>.
- [16] T.H. Lee, C.S. Oh, S.J. Kim, Scripta Mater., 58 (2) (2008) 110-113.
- [17] H.Y. Ha, T.H. Lee, S.J. Kim, Electrochim. Acta, 80 (2012) 432-439.
- [18] Z.P. Shi, Z.B. Wang, J.Q. Wang, Y.X. Qiao, H.N. Chen, T.Y. Xiong, Y.G. Zheng, Acta Metall. Sin. (Engl. Lett.) 33 (3) (2020) 415-424.
- [19] C.S. Huang, C.C. Shih, Mater. Sci. Eng. A, 402 (1-2) (2005) 66-75.
- [20] M. Milititsky, N.D. Wispelaere, R. Petrov, J.E. Ramos, A. Reguly, H. Hänninen, Mater. Sci. Eng. A, 498 (1-2) (2008) 289-295.
- [21] C. Herrera, D. Ponge, D. Raabe, Acta Mater., 59 (11) (2011) 4653-4664.
- [22] U. Gürol, K. Can, J. Min. Metall. Sect. B-Metall., 56 (2) (2020) 171-182.
- [23] D.B. Wei, H.X. Liang, S.Q. Li, F.K. Li, F. Ding, S.Y. Wang, Z.L. Liu, P.Z. Zhang, J. Min. Metall. Sect. B-Metall. 55 (2) (2019) 227-234.
- [24] H. Zhao, Y. Ren, J. Dong, K. Yang, Materialwiss. Werkst., 49 (12) (2018) 1439-1448.
- [25] H.C. Zhao, Y.B. Ren, J.H. Dong, X.M. Fan, K. Yang, Acta Metall. Sin. (Engl. Lett.) 29 (3) (2016) 217-227.
- [26] V. Vats, T. Baskaran, S.B. Arya, Tribol. Int., 119 (2018) 659-666.
- [27] D.J. Mills, R.D. Knutsen, Wear, 215 (1998) 83-90.
- [28] H.L. Ming, X.C. Liu, J. Lai, J.Q. Wang, L.X. Gao, E.H. Han, J. Nucl. Mater., 529 (2020) 151930.
- [29] J. Dib, S. Hereñu, D. Alí, N. Pellegrini, J. Mater. Eng. Perform., 29 (5) (2020) 2739-2747.
- [30] H. Torres, M. Varga, K. Adam, M. R. Ripoll, Wear, 364-365 (2016) 73-83.
- [31] J. Marteau, S. Bouvier, M. Bigerelle, Arch. Comput. Method. Eng., 22 (4) (2015) 577-593.
- [32] Y.X. Qiao, J. Chen, H.L. Zhou, Y.X. Wang, Q.N. Song, H.B. Li, Z.B. Zheng, Wear, 424-425 (2019) 70-77.
- [33] Y. Lu, D. Zhou, X. Li, J. Wang, W. Li, Z. Bai, Mater. Tehnol., 52 (5) (2018) 673-678.
- [34] L.M. Zhang, Z.X. Li, J.X. Hu, A.L. Ma, S. Zhang, E.F. Daniel, A.J. Umoh, H.X. Hu, Y.G. Zheng, Tribol. Int.,



- 155 (2021) 106752,
- [35] K.H. Lo, C.H. Shek, J.K.L. Lai, Mater. Sci. Eng. R, 65 (4-6) (2009) 39-104.
- [36] H.B. Li, Z.H. Jiang, Z.R. Zhang, Y. Yang, J. Iron Steel Res. Int., 16 (1) (2009) 58-61.
- [37] W.C. Oliver, G.M. Pharr, J. Mater. Res., 7 (6) (2011) 1564-1583.
- [38] Y.T. Xi, Y.Y. Bai, K.W. Gao, X.L. Pang, H.S. Yang, L.C. Yan, A.A. Volinsky, Ceram. Int., 44 (13) (2018) 15851-15858.
- [39] A.P. Tschiptschin, C.M. Garzón, D.M. Lopez, Tribol. Int., 39 (2) (2006) 167-174.
- [40] L. Wang, A.K. Tieu, S.G. Cui, G.U. Deng, P. Wang, H.T. Zhu, J. Yang, Tribol. Int., 142, (2020) 105972.
- [41] Q.Y. Zhang, H.Y. Ding, G.H. Zhou, L.C. Zhang, Q.M. Chen, K. Qin, Y.J. Dai, Tribology, 37 (6) (2017) 823-830.
- [42] Y.J. Cao, J.Q. Sun, F. Ma, Y.Y. Chen, X.Z. Cheng, X. Gao, K. Xie, Tribol. Int., 115 (2017) 108-115.
- [43] Z. X. Chen, H. X. Hu, Y. G. Zheng, X. M. Guo, Wear, 466-467 (2021) 203561.
- [44] P. Hedenqvist, S. Hogmark, Tribol. Int., 30 (7) (1997) 507-516.
- [45] S.C. Lim, M.F. Ashby, Acta Metall., 35 (1) (1987) 1-24.
- [46] T. Savaşkan, O. Bican, Tribol. Int., 43 (8) (2010) 1346-1352.
- [47] M. Fellah, L. Aissani, M. Abdul Samad, A. Iost, T. Mohamed Zine, A. Montagne, C. Nouveau, Acta Metall. Sin. (Engl. Lett.), 30 (11) (2017) 1089-1099.
- [48] W.T. Fu, Y.Z. Zheng, X.K. He, Wear, 249 (2001) 788-791.
- [49] X.R. Zhang, S.C. Sun, G.X. Sun, S. Han, Z.H. Jiang, J.S. Lian, Mater. Sci. Tech., 35 (13) (2019) 1592-1599.
- [50] Q. Li, J. Guo, A.M. Zhao, Tribol. Lett., 67 (4) (2019) 121.
- [51] Y.L. Song, C. Yu, X. Miao, X.H. Han, D.S. Qian, X. Chen, Acta Metall. Sin. (Engl. Lett.), 30 (10) (2017) 957-964.
- [52] B.J. Choi, I.S. Cho, D.H. Jung, M.G. Lee, Y.H. Jeon, Arch. Metall. Mater. 64 (3) (2019) 841-844.
- [53] S.M. Hsu, M.C. Shen, A.W. Ruff, Tribol. Lett., 30 (5) (1997) 377-383.
- [54] Y.S. Mao, L. Wang, K.M. Chen, S.Q. Wang, X.H. Cui, Wear, 297 (1-2) (2013) 1032-1039.
- [55] H.C. Zhao, Y.B. Ren, W.P. Liu, X.M. Fan, K. Yang, Chinese J. Mater. Res., 30 (3) (2016) 171-178.
- [56] D.T. Llewellyn, Mater. Sci. Tech., 13 (5) (2013) 389-400.
- [57] Q.Y. Zhang, Y. Zhou, L. Wang, X.H. Cui, S.Q. Wang, Tribol. Int., 94 (2016) 541-549.
- [58] J. Dib, S. Hereñu, D. Alí, N. Pellegrini, J. Mater. Eng. Perform., 29 (5) (2020) 2739-2747.
- [59] I.M. Zylla, H.P. Hougardy, Steel Res. Int., 65 (4) (1994) 132-137.
- [60] D.S. Lu, Z.Y. Liu, W. Li, Z. Liao, H. Tian, J.Z. Xian, China Foundry, 12 (1) (2015) 39-47.
- [61] A. Sébastien, P.C. Jean, B. Olivier, Steel Res. Int., 73 (6-7) (2002) 299-302.
- [62] Y.N. Dastur, W.C. Leslie, Metall. Mater. Trans. A, 12 (5) (1981) 749-759.
- [63] T.H. Lee, C.S. Oh, S.J. Kim, S. Takaki, Acta Mater., 55 (11) (2007) 3649-3662.
- [64] M. Ojima, Y. Adachi, Y. Tomota, K. Ikeda, T. Kamiyama, Y. Katada, Mater. Sci. Eng. A, 527 (1-2) (2009) 16-24.

PONAŠANJE AUSTENITNOG NERĐAJUĆEG ČELIKA SA VISOKIM SADRŽAJEM AZOTA Fe-19Cr-15Mn-0.66N PRI TRENJU I HABANJU

Y.-X. Qiao^{a,*}, S.-L. Sheng^a, L.-M. Zhang^b, J. Chen^{a,*}, L.-L. Yang^a,
H.-L. Zhou^a, Y.-X. Wang^a, H.-B. Li^c, Z.-B. Zheng^{d,*}

^a Fakultet za nauku o materijalima i inženjerstvo materijala, Univerzitet nauke i tehnologije u Đangsuu, Džedang, Kina

^b CAS glavna laboratorija za nuklearni materijal i procenu bezbednosti, Institut za istraživanje metala, Kineska akademija nauka, Šenjang, Kina

^c Metalurški fakultet, Severnoistočni univerzitet, Šenjang, Kina

^d Glavna laboratorija za tehnologiju kaljenja metala i njihovu primenu u Guandongu, Institut za materijale i njihovu preradu u Guandongu, Guangžu, Kina

Apstrakt

Istraživano je ponašanje austenitnog nerđajućeg čelika (HNSS) sa visokim sadržajem azota Fe-19Cr-15Mn-0.66N pri trenju i habanju. Tribološka ispitivanja su izvršena pod različitim opterećenjima od 5 N, 10 N, 15 N i 20 N. Da bi se razumeo mehanizam habanja pod različitim opterećenjima kao i razlozi za veću otpornost na habanje korišćeni su elektronski skenirajući mikroskop (SEM) i konfokalni lasersko-skenirajući mikroskop (LSMC). Uočeni su niži koeficijent trenja i veća otpornost na habanje sa povećanjem opterećenja. Pod većim opterećenjem, trenje je povećalo sposobnost očvršćavanja HNSS što je poboljšalo njegovu površinsku tvrdoću, i na taj način otpornost na habanje HNSS je porasla.

Ključne reči: Austenitni nerđajući čelik sa visokim sadržajem azota; Habanje; Očvršćavanje; Koeficijent trenja

